Available online at www.sciencedirect.com
ScienceDirect
International Journal of Heat and Fluid Flow 28 (2007) 161–177
International Journal of HEAT AND FLUID FLOW
www.elsevier.com/locate/ijhff

An evaluation of bypass transition models for turbomachinery flows

L. Cutrone, P. De Palma, G. Pascazio, M. Napolitano *

Dipartimento di Ingegneria Meccanica e Gestionale, DIMeG, Centro di Eccellenza in Meccanica Computazionale, CEMeC, Politecnico di Bari, Via Re David 200, 70125 Bari, Italy

Received 29 July 2005; received in revised form 16 January 2006; accepted 21 February 2006
Available online 30 June 2006

Abstract

This paper provides a thorough analysis of six laminar-to-turbulent bypass transition models. Five models are obtained by combining a transition-onset correlation with an intermittency-factor models, whereas the sixth one is a single-point model based on the use of a laminar kinetic energy transport equation. All models have been embedded in a Reynolds averaged Navier–Stokes solver employing a low Reynolds number k–ω turbulence model. The performance of the transition models have been evaluated by computing three well documented incompressible flows past flat plates, namely, tests T3A, T3B, and T3C2 of ERCOFTAC SIG 10, with different free-stream conditions, the last one being characterized by a non-zero pressure gradient. Finally, a more complex test case has been considered, for which detailed experimental data are available in the literature, namely, the two-dimensional flow through a turbine cascade.

Keywords: Bypass transition; Intermittency; RANS equations

1. Introduction

During the last decades, the role of computational fluid dynamics (CFD) in the development of modern turbomachinery has become more and more important, insofar as it can be routinely employed to reduce design time and costs and it can also be employed to achieve a deeper understanding of the basic physics of complex-flow phenomena, which are crucial to design improved engines. Therefore, the validation of the numerical models and their application to flow configurations of increasing complexity is of great interest. In particular, one of the most challenging problems when developing accurate computational tools is the laminar-to-turbulent boundary-layer transition, whose role in gas turbine engines is widely recognized (Mayle, 1991).

In many turbomachinery flows, although the main stream can be highly turbulent, the boundary layers may be either laminar or turbulent and transition mainly occurs bypassing the "natural" amplification of Tollmien–Schlichting waves, due to the typical high level of free-stream turbulence intensity. The performance of turbines (especially low-pressure ones) and compressors can be highly influenced by transition: in many cases, it may be crucial for the generation of large separation regions, which have a remarkable impact on losses, and for the heat-transfer phenomenon. Therefore, the modeling of transition represents a fundamental issue for the improvement of the performance of modern turbomachinery, but it is also a formidable task to achieve because the transition process involves a wide range of scales and it is very sensitive to physical flow features, such as pressure gradients and free-stream turbulence. The basic mechanism of boundary-layer transition under different flow conditions can be studied using direct numerical simulations and large eddy simulations for low to moderate values of the Reynolds number. Unfortunately, due to their prohibitive computational cost, such techniques

* Corresponding author. Tel.: +39 0805963464; fax: +39 0805963411.
E-mail addresses: cutrone@imedado.poliba.it (L. Cutrone), depalma@poliba.it (P. De Palma), pascazio@poliba.it (G. Pascazio), napolita@poliba.it (M. Napolitano).

0142-727X/$ - see front matter © 2006 Elsevier Inc. All rights reserved.
doi:10.1016/j.ijheatfluidflow.2006.02.031

Nomenclature

C_f	skin-friction coefficient, $C_f = \tau_w/(1/2u_\infty^2\rho_\infty)$
D	diffusion term, source term
H	specific total enthalpy
H_{12}	shape factor
K	acceleration parameter, $(\nu/u^2)(du/dx)$
k	turbulence kinetic energy
n	spot generation rate
$\hat{n}$	dimensionless spot generation rate
P	production term
p	pressure
Q	conservative variable vector
Q_v	primitive variable vector
Re_θ	momentum thickness Reynolds number, $Re_\theta = (\theta u_\infty)/\nu$
S	source term
S_{ij}	strain-rate-tensor components
T	temperature
t	time
Tu	turbulence intensity ($Tu = 100\sqrt{2k/3u_\infty^2}$)
U	specific total internal energy
u	velocity magnitude
u_i, u_j	velocity components
u_∞	local free-stream speed
u_{in}	inlet velocity
u^+	u/u_τ
u_τ	friction velocity, $u_\tau = \sqrt{\tau_w/\rho}$
x	curvilinear coordinate
y^+	$(y_n u_\tau)/\nu$
y_n	normal distance to wall
δ	boundary-layer thickness
δ_{ij}	Kronecker delta
ε	turbulence dissipation rate
γ	intermittency factor
λ	turbulence length scale
λ_θ	Thwaites' pressure gradient parameter
θ	momentum thickness
μ	molecular viscosity
μ_T	eddy viscosity
$\mu_T^\star$	$\gamma\mu_T$
ν	μ/ρ
ν_T	μ_T/ρ
ρ	density
σ	Emmos spot propagation parameter
τ_{ij}	stress-tensor components
ω	specific dissipation rate

Subscripts

in	inlet
is	isentropic
L	laminar
le	leading edge
T	turbulent
t	onset of transition, turbulent
∞	free stream

Superscripts

r	pseudo-time level
n	physical-time level

are not feasible for the high Reynolds numbers and the complex geometries encountered in most turbomachinery flows. In such cases, numerical models based on the solution of the Reynolds averaged Navier–Stokes (RANS) equations are needed. These models are capable of predicting with a good level of accuracy only the mean fluid- and thermo-dynamic variables and they can achieve a good level of reliability for the prediction of specific complex-flow configurations employing turbulence models based on transport equations. However, notwithstanding the efforts of several researchers aimed at developing low Reynolds number turbulence models with some built-in transition modeling capability, they have been proven inadequate for predicting the transition under general flow conditions (Savill, 2002a; Westin and Henkes, 1997; De Palma, 2002). Recent research activity aims at developing transition models based either on non-linear eddy viscosity methods (Craft et al., 1997; Chen et al., 1998) and Reynolds-stress transport equations (Hanialić et al., 1997), or on the concept of intermittency, which represents the fraction of time the flow is turbulent (Mayle, 1991). Craft et al. (1997) have shown that using a low-*Re* k–ε turbulence model with either a two- or a three-equation non-linear approach can provide accurate results for the T3A and T3B test cases, see also Chen et al. (1998) and Savill (2002a). In fact, as reported by Chen et al. (1998), such non-linear models "return a more credible representation of transition than the linear variant"; however, results for test cases with non-zero pressure gradient do not provide an improvement over linear eddy viscosity models. These numerical experiments led Chen et al. (1998) to the conclusion that "none of the models may be said to be entirely satisfactory". The level of closure provided by the Reynolds-stress transport models certainly offers a more general framework to predict complex turbulent flows and transition. Also for this kind of models the tuning of the coefficients may have a remarkable impact on the results (Hanialić et al., 1997). Furthermore, the combination of low-*Re* Reynolds-stress transport models with an intermittency transport equation has recently been proposed with success, as reported by Savill (2002b). However, the required computational cost of such models is larger than that required by linear and non-linear eddy viscosity models. Therefore, this paper will focus on models based on the intermittency concept in conjunction with a linear eddy viscosity model. The most common way to couple

the transition model with the turbulence one is to multiply the eddy viscosity coefficient by the intermittency coefficient, although such a simple approach could produce considerable errors in the calculations of the shear stresses (Mayle, 1991). Therefore, several methods have been proposed to compute the intermittency coefficient, being based on empirical algebraic correlations (Mayle, 1991; Michelassi et al., 1999) or on the solution of an additional transport equation (Cho and Chung, 1992; Suzen and Huang, 2000; Steelant and Dick, 1996). One disadvantage of intermittency type models is that they rely on integral or non-local parameters, such as boundary-layer thickness and momentum thickness, which are difficult to evaluate in complex geometry configurations. In order to overcome such a drawback, Walters and Leylek (2004) provided a single-point transition model, which does not depend on the intermittency factor: following the approach originally proposed by Mayle and Schulz (1997), they model the pretransitional stream-wise boundary-layer fluctuations induced by the free-stream turbulence, by introducing an additional transport equation for the laminar kinetic energy.

In this paper, the low Reynolds number k–ω turbulence model (Wilcox, 1998), already employed by the authors for the solution of the RANS equations (De Palma et al., 2001), has been embedded in a multi-block solver for the preconditioned compressible RANS equations to provide an accurate, efficient and versatile tool for studying complex flows of industrial interest. Six transition models have been considered: three of them are based on combinations of algebraic correlations (Abu-Ghannam and Shaw, 1980; Suzen and Huang, 2000); two of them are obtained combining an algebraic correlation to predict the transition onset with two different intermittency transport models (Steelant and Dick, 1996; Suzen and Huang, 2000); and the last one employs a transport equation for the laminar kinetic energy (Walters and Leylek, 2004). The last model has been extended to the computation of compressible flows and has been validated, for the first time to the authors' knowledge, versus well known basic test cases provided by ERCOFTAC and a complex flow through a turbomachinery cascade.

2. Flow equations and turbulence model

The Reynolds averaged Navier–Stokes (RANS) equations, written in terms of Favre mass-averaged variables and using the low Reynolds number k–ω turbulence model, are written as follows:

$$\frac{\partial \rho}{\partial t}+\frac{\partial}{\partial x_j}(\rho u_j)=0, \tag{1}$$

$$\frac{\partial(\rho u_i)}{\partial t}+\frac{\partial}{\partial x_j}(\rho u_j u_i)=-\frac{\partial p}{\partial x_i}+\frac{\partial \hat{\tau}_{ij}}{\partial x_j}, \tag{2}$$

$$\frac{\partial(\rho U)}{\partial t}+\frac{\partial}{\partial x_j}(\rho u_j H)=\frac{\partial}{\partial x_j}\left[u_i\hat{\tau}_{ij}+(\mu+\sigma^*\mu_{\mathrm{T}})\frac{\partial k}{\partial x_j}-q_j\right], \tag{3}$$

$$\frac{\partial(\rho k)}{\partial t}+\frac{\partial}{\partial x_j}(\rho u_j k)=\tau_{ij}\frac{\partial u_i}{\partial x_j}-\beta^*\rho\omega k+\frac{\partial}{\partial x_j}\left[(\mu+\sigma^*\mu_{\mathrm{T}})\frac{\partial k}{\partial x_j}\right], \tag{4}$$

$$\frac{\partial(\rho\omega)}{\partial t}+\frac{\partial}{\partial x_j}(\rho u_j \omega)=\frac{\alpha\omega}{k}\tau_{ij}\frac{\partial u_i}{\partial x_j}-\beta\rho\omega^2+\frac{\partial}{\partial x_j}\left[(\mu+\sigma\mu_{\mathrm{T}})\frac{\partial \omega}{\partial x_j}\right]. \tag{5}$$

In the equations above, U and H are the specific total energy and enthalpy, respectively, both including the turbulence kinetic energy, k; the eddy viscosity, μ_{T}, is defined in terms of k and of the specific dissipation rate, ω, according to the k–ω turbulence model of Wilcox (1998), namely:

$$\mu_{\mathrm{T}}=\alpha^*\frac{\rho k}{\omega}. \tag{6}$$

Moreover, $\hat{\tau}_{ij}$ indicate the sum of the molecular and Reynolds (τ_{ij}) stress-tensor components. According to the Boussinesq approximation, one has:

$$\hat{\tau}_{ij}=(\mu+\mu_{\mathrm{T}})\left[\frac{\partial u_i}{\partial x_j}+\frac{\partial u_j}{\partial x_i}-\frac{2}{3}\frac{\partial u_k}{\partial x_k}\delta_{ij}\right]-\frac{2}{3}\rho k\delta_{ij}. \tag{7}$$

Finally, the heat flux vector components, q_j, are given as:

$$q_j=-\left(\frac{\mu}{Pr}+\frac{\mu_{\mathrm{T}}}{Pr_{\mathrm{T}}}\right)\frac{\partial h}{\partial x_j}, \tag{8}$$

where $Pr=0.71$ and $Pr_{\mathrm{T}}=1$ are the laminar and turbulent Prandtl numbers, respectively. Sutherland's law is used to compute the molecular viscosity coefficient and the low-Reynolds-number coefficients are used for the k–ω model, see Wilcox (1998) for details.

3. Laminar-to-turbulent transition

In this section, a detailed description of the transition models employed in the present work is provided. Firstly, two algebraic correlations employed to predict the transition onset are presented and then five transition models are described, obtained combining such correlations with different intermittency models. All of these models are based on the evaluation of the intermittency factor (namely, the probability that the flow is locally turbulent), γ, which is used to compute the eddy viscosity coefficient, $\mu_{\mathrm{T}}^{\bigstar}=\gamma\mu_{\mathrm{T}}$, employed instead of μ_{T} in the flow and turbulence-model equations. Finally, the sixth model is described, which is a single-point transition model based on a transport equation for the laminar kinetic energy.

3.1. Transition-onset correlations

3.1.1. Abu-Ghannam and Shaw (C1)

The correlation proposed Abu-Ghannam and Shaw (1980) is a well known algebraic model based on experimental measurements of flows over flat plates. It evaluates a critical value for the Reynolds number based on the boundary-layer momentum thickness, which indicates the location of the transition onset (Abu-Ghannam and Shaw, 1980):

$$Re_{\theta_t} = 163 + \exp\left(F(\lambda_\theta) - \frac{F(\lambda_\theta)Tu_{le}}{6.91}\right), \quad (9)$$

where Tu_{le} is the free-stream value of Tu at the leading edge section and $\lambda_\theta = (\theta^2/\nu_\infty)\mathrm{d}u_\infty/\mathrm{d}x$ is the pressure gradient parameter, u_∞ being the local free-stream speed. It is noteworthy that the edge of the boundary layer is defined as the point at which $u = 0.99u_{in}$, for the test cases characterized by zero pressure gradient; otherwise, it is the first grid point away from the wall at which the speed increases less than 1% with respect to its value at the previous grid point. The function F is given as:

$$F(\lambda_\theta) = \begin{cases} 6.91 + 12.75\lambda_\theta + 63.64\lambda_\theta^2 & \text{if } \lambda_\theta < 0, \\ 6.91 + 2.48\lambda_\theta - 12.27\lambda_\theta^2 & \text{if } \lambda_\theta \geqslant 0. \end{cases} \quad (10)$$

3.1.2. Suzen et al. (C2)

The following correlation has been proposed by Suzen et al. (2002) for evaluating Re_{θ_t}:

$$Re_{\theta_t} = \left(120 + 150Tu_{le}^{-2/3}\right)\coth[4(0.3 - |K_{min}| \times 10^5)]. \quad (11)$$

In the equation above K_{min} indicates the smallest value of the pressure gradient parameter $K_\infty = (\nu_\infty/u_\infty^2)(\mathrm{d}u_\infty/\mathrm{d}x)$ in the deceleration region, evaluated at the local edge of the boundary layer. According to the correlations provided by Mayle (1991), the maximum value for $|K_{min}|$ is 3×10^{-6}.

3.2. Transition models

3.2.1. Model 1 (M1)

The first transition model (M1) is obtained using the transition-onset correlation C1 together with the general Dhawan and Narasimha correlation for the intermittency factor (Dhawan and Narasimha, 1958),

$$\gamma = 1 - \exp[-\hat{n}\sigma(Re_x - Re_{x_t})^2], \quad (12)$$

where x is the curvilinear coordinate along the wall, $Re_x = u_\infty x/\nu_\infty$, $\hat{n} = n\nu_\infty^2/u_\infty^3$ is the non-dimensional production rate parameter of the turbulent spots, ν is the kinematic viscosity, and σ is the Emmos parameter which depends on the shape and velocity of the turbulent spots. In Eq. (12) the spot production parameter $\hat{n}\sigma$ has been computed as (Mayle, 1991):

$$\hat{n}\sigma = 1.5 \times 10^{-11} Tu_\infty^{7/4}, \quad (13)$$

where Tu_∞ is the local free-stream value of Tu, evaluated as $Tu_\infty = Tu_{le,\infty}(u_{le,\infty}/u_\infty)^{3/2}$.

3.2.2. Model 2 (M2)

In the presence of a pressure gradient, correlation (13) for the spot production rate is corrected as

$$\hat{n}\sigma = (\hat{n}\sigma)_{ZPG}\mathrm{PRC}, \quad (14)$$

where $(\hat{n}\sigma)_{ZPG}$ is the production rate for zero pressure gradient (ZPG), and PRC accounts for the influence of the pressure gradient through the value of the parameter K_∞. From the data of Mayle (1991), Steelant and Dick (1996) provided the following correlation:

$$\mathrm{PRC} = \begin{cases} (474Tu_{le}^{-2.9})^{1-\exp(2\times10^6 K_\infty)}, & K_\infty < 0, \\ 10^{-3227K_\infty^{0.5985}}, & K_\infty \geqslant 0, \end{cases} \quad (15)$$

where Tu_{le} is the free-stream value of Tu at the leading edge section.

The second model (M2) is obtained combining the transition-onset correlation C1 with Eqs. (12), (14), and (15).

3.2.3. Model 3 (M3)

Transition model M3 employs the transition-onset correlation C2 and the previous spot production rate corrected with the coefficient PRC.

3.2.4. Modified Steelant and Dick model (M4)

Steelant and Dick (1996) proposed a model for bypass transition based on the correlation (12). Assuming a Gaussian distribution for $\hat{n}\sigma(Re_x - Re_{x_t})^2$ in the transition region, centered at the point of the transition onset, x_t, they provided the following transport equation for the intermittency factor:

$$\frac{\partial(\rho\gamma)}{\partial t} + \frac{\partial(\rho u_j\gamma)}{\partial x_j} = (1-\gamma)\beta(x)\rho\sqrt{u_k u_k}, \quad (16)$$

where $\beta(x) = 2f(x)f'(x)$, $f'(x)$ being the derivative of $f(x)$. $f(x)$ is the following polynomial interpolation function for $\hat{n}\sigma(Re_x - Re_{x_t})^2$ around the point x_t of transition onset (Steelant and Dick, 1996):

$$f(x) = \frac{ax'^4 + bx'^3 + cx'^2 + dx' + e}{h_1 x' + h_2} \quad (17)$$

with $x' = x - x_t$, and

$$a = 50\sqrt{\frac{n\sigma}{u}}, \quad b = -0.4906, \quad c = 0.204\left(\frac{n\sigma}{u}\right)^{-0.5},$$
$$d = 0, \quad e = 0.04444\left(\frac{n\sigma}{u}\right)^{-1.5}, \quad h_1 = 50, \quad h_2 = 10e. \quad (18)$$

The values of the coefficients a and h_1 are the ones provided by Suzen and Huang (2000) in order to adapt the model originally proposed by Steelant and Dick for the conditioned Navier–Stokes equations to the RANS equations. The value of $\hat{n}\sigma$ is estimated using a modified version of the correlation (13), namely,

$$\hat{n}\sigma = 1.8 \times 10^{-11} Tu_\infty^{7/4}. \quad (19)$$

The intermittency transport model of Steelant and Dick combined with the transition-onset correlation C2 is referred to as M4.

3.2.5. Suzen and Huang model (M5)

Suzen and Huang (2000) proposed a transition model consisting in one transport equation for the intermittency factor based on the correlation of Dhawan and Narasimha, Eq. (12), for the intermittency distribution along the flow

direction. This model provides the distribution of the intermittency factor along the normal direction to the wall. To this end, it combines the model of Steelant and Dick (1996) with the model of Cho and Chung (1992) employing a blending function. The transport equation for the intermittency factor, γ, reads:

$$\frac{\partial(\rho\gamma)}{\partial t}+\frac{\partial(\rho u_j\gamma)}{\partial x_j}=D_\gamma+S_\gamma, \tag{20}$$

where D_γ is the diffusion term, namely,

$$D_\gamma=\frac{\partial}{\partial x_j}\left\{\left[(1-\gamma)\gamma\sigma_{\gamma_L}\mu+(1-\gamma)\sigma_{\gamma_T}\mu_T\right]\frac{\partial\gamma}{\partial x_j}\right\}, \tag{21}$$

and

$$S_\gamma=(1-\gamma)[(1-F)T_0+F(T_1-T_2)]+T_3, \tag{22}$$

where F is a blending function. The first term, T_0, derives from the model of Steelant and Dick (1996),

$$T_0=C_0\rho\sqrt{u_ku_k}\beta(x), \tag{23}$$

where $\beta(x)=2f(x)f'(x)$ and the function $f(x)$ is given by Eq. (17) with the coefficients (18). The T_1, T_2 and T_3 terms are derived from the model of Cho and Chung (1992) and are given respectively as:

$$T_1=\frac{C_1\gamma}{k}\tau_{ij}\frac{\partial u_i}{\partial x_j}, \tag{24}$$

$$T_2=C_2\gamma\rho\frac{k^{1/2}}{\beta^*\omega}\frac{u_i}{\sqrt{u_ku_k}}\frac{\partial u_i}{\partial x_j}\frac{\partial\gamma}{\partial x_j}, \tag{25}$$

$$T_3=C_3\rho\frac{k}{\beta^*\omega}\frac{\partial\gamma}{\partial x_j}\frac{\partial\gamma}{\partial x_j}. \tag{26}$$

The blending function, F, provides a smooth passage between the two models in the transition region. It is evaluated as a function of the ratio $k/(Sv)$, where $S=\sqrt{2S_{ij}S_{ij}}$, and is given as:

$$F=\tanh^4\left[\frac{k/(Sv)}{200(1-\gamma^{0.1})^{0.3}}\right]. \tag{27}$$

The above equation is based on the correlation due to Klebanoff for the distribution of γ in the normal direction to the wall, and it renders active the model of Steelant and Dick (1996) close to the wall, whereas it applies the model of Cho and Chung in the outer region. The values of the coefficients employed for the present model are:

$$\begin{cases}\sigma_{\gamma_L}=1, & \sigma_{\gamma_T}=1,\\ C_0=1, & C_1=1.6, \quad C_2=0.16, \quad C_3=0.15.\end{cases} \tag{28}$$

The intermittency transport model of Suzen and Huang combined with the transition-onset correlation C2 is referred to as M5.

3.2.6. Walters and Leylek model (M6)

This model is a modified version of the original model presented by Walters and Leylek (2004, 2005), suitable for compressible flow calculations. The model is based on an eddy viscosity coefficient, determined by using three transport equations for the turbulence kinetic energy, k, the laminar kinetic energy, k_L, and the specific dissipation rate, ω, respectively:

$$\frac{\partial(\rho k)}{\partial t}+\frac{\partial}{\partial x_j}(\rho u_jk)=\rho P_k+\rho R-\rho\varepsilon-\rho D_T+\frac{\partial}{\partial x_j}\left[\left(\mu+\frac{\rho\alpha_T}{\sigma_k}\right)\frac{\partial k}{\partial x_j}\right], \tag{29}$$

$$\frac{\partial(\rho k_L)}{\partial t}+\frac{\partial}{\partial x_j}(\rho u_jk_L)=\rho P_{k_L}-\rho R-\rho D_L+\frac{\partial}{\partial x_j}\left[\mu\frac{\partial k_L}{\partial x_j}\right], \tag{30}$$

$$\frac{\partial(\rho\omega)}{\partial t}+\frac{\partial}{\partial x_j}(\rho u_j\omega)=\rho P_\omega+\rho C_{\omega R}\frac{\omega}{k}R-\rho C_{\omega2}\omega^2+\rho C_{\omega2}f_\omega\alpha_T\left(\frac{\lambda_{eff}}{\lambda_T}\right)^{4/3}\frac{\sqrt{k}}{y_n^3}+\frac{\partial}{\partial x_j}\left[\left(\mu+\frac{\rho\alpha_T}{\sigma_\omega}\right)\frac{\partial\omega}{\partial x_j}\right]. \tag{31}$$

Eqs. (29) and (31) substitute the equations of the original turbulence model, namely, Eqs. (4) and (5), respectively. The laminar kinetic energy represents the magnitude of the "non-turbulent" stream-wise fluctuations in the pre-transitional boundary layer, defined in the work of Mayle and Schulz (1997). The effective length scale, λ_{eff}, is the minimum length scale of the eddies contributing to the production of these non-turbulent fluctuations by means of the splat mechanism described by Walters and Leylek (2005) and Volino (1998). It is estimated as

$$\lambda_{eff}=\min(C_\lambda y_n,\lambda_T), \tag{32}$$

where $C_\lambda=2.495$, $\lambda_T=k^{3/2}/\varepsilon$ is the turbulence length scale, $\varepsilon=\omega k$ is the turbulence dissipation rate, and y_n is the distance from the nearest wall. The turbulence kinetic energy can be divided into a large-scale energy, $k_{T,l}$, and a small-scale energy, $k_{T,s}$, as follows

$$k_{T,s}=k(\lambda_{eff}/\lambda_T)^{2/3}, \quad k_{T,l}=k\left[1-(\lambda_{eff}/\lambda_T)^{2/3}\right]; \tag{33}$$

the former one interacts with the mean flow as a typical turbulence energy, whereas the latter one contributes to the production of k_L.

The first term on the right-hand side of Eq. (29) is the production of turbulence due to turbulent fluctuations

$$P_k=\nu_{T,s}\left(\frac{\partial u_i}{\partial x_j}+\frac{\partial u_j}{\partial x_i}-\frac{2}{3}\frac{\partial u_k}{\partial x_k}\delta_{ij}\right)\frac{\partial u_i}{\partial x_j}-\frac{2}{3}k_{T,s}\frac{\partial u_k}{\partial x_k}, \tag{34}$$

where the small-scale viscosity, $\nu_{T,s}$, is defined as

$$\nu_{T,s}=\min\left(f_\mu f_{INT}C_\mu\sqrt{k_{T,s}}\lambda_{eff},\frac{2.5\varepsilon_{TOT}}{S^2}\right). \tag{35}$$

In the above equation, C_μ is the turbulent viscosity coefficient, taken to be 0.09 in fully turbulent regions, and f_μ and f_{INT} are damping functions used to impose near-wall viscous effects and to prevent the overprediction of momentum in the latter stages of bypass transition, respectively. The functional form of these coefficients is reported in detail by Walters and Leylek (2004, 2005).

The first term on the right-hand side of Eq. (30) is the production of the laminar kinetic energy due to large-scale turbulent fluctuations,

$$P_{k_L} = \nu_{T,l}\left(\frac{\partial u_i}{\partial x_j}+\frac{\partial u_j}{\partial x_i}-\frac{2}{3}\frac{\partial u_k}{\partial x_k}\delta_{ij}\right)\frac{\partial u_i}{\partial x_j}-\frac{2}{3}k_{T,l}\frac{\partial u_k}{\partial x_k}. \quad (36)$$

The large-scale viscosity $\nu_{T,l}$ is defined as

$$\nu_{T,l} = \min\left[f_{\tau,l}C_{ll}\left(\frac{\Omega\lambda_{eff}^2}{\nu}\right)\sqrt{k_{T,l}}\lambda_{eff}, \frac{0.5k_{T,l}}{S}\right], \quad (37)$$

where $f_{\tau,l}$ is a time-scale-based damping function (Walters and Leylek, 2004).

The term R in Eqs. (29)–(31) represents the effect of the stream-wise fluctuations onto turbulence during bypass transition,

$$R = C_R\beta_{BP}k_L\omega\left(\frac{\lambda_T}{\lambda_{eff}}\right), \quad (38)$$

where β_{BP} is a threshold function defined as

$$\beta_{BP} = 1-\exp\left(-\frac{\phi_{BP}}{A_{BP}}\right), \quad \phi_{BP} = \max\left[\left(\frac{\sqrt{k}y_n}{\nu}-C_{BP,crit}\right),0\right]. \quad (39)$$

The terms D_T and D_L in Eqs. (29) and (30) are the turbulent and laminar near-wall dissipation terms, respectively, and they are given as (Walters and Leylek, 2004)

$$D_T = 2\nu\frac{\partial\sqrt{k}}{\partial x_j}\frac{\partial\sqrt{k}}{\partial x_j}, \quad D_L = 2\nu\frac{\partial\sqrt{k_L}}{\partial x_j}\frac{\partial\sqrt{k_L}}{\partial x_j}. \quad (40)$$

According to these definitions, the total dissipation rate of the fluctuation energy, ε_{TOT}, is defined as the sum of the dissipation rate of turbulence, ε, and of the near-wall dissipation terms, D_T and D_L.

The production term P_ω in Eq. (31) takes the form

$$P_\omega = \frac{\omega}{k}C_{\omega1}\left[\nu_{T,\omega}\left(\frac{\partial u_i}{\partial x_j}+\frac{\partial u_j}{\partial x_i}-\frac{2}{3}\frac{\partial u_k}{\partial x_k}\delta_{ij}\right)\frac{\partial u_i}{\partial x_j}-\frac{2}{3}k_{T,s}\frac{\partial u_k}{\partial x_k}\right], \quad (41)$$

where $\nu_{T,\omega}$ corresponds to the small-scale viscosity in Eq. (35) without any imposed limit. The coefficients $C_{\omega R}$ and $C_{\omega2}$ in Eq. (31) are assigned according to the following functional form

$$C_{\omega R} = 1.5\left(\frac{\lambda_T}{\lambda_{eff}}\right)^{2/3}-1 \quad \text{and} \quad C_{\omega2} = 0.92\left(\frac{\lambda_{eff}}{\lambda_T}\right)^{4/3}. \quad (42)$$

Finally, the turbulence scalar diffusivity in Eqs. (29) and (31) is defined as

$$\alpha_T = f_v C_{\mu,std}\sqrt{k}\lambda_{eff}. \quad (43)$$

The numerical values of the model constants are reported by Walters and Leylek (2005) and are omitted in this work for the sake of brevity.

The influence of turbulent and laminar fluctuations on the mean flow and energy equations is accounted for by defining a total eddy viscosity which is used to model the Reynolds stress tensor in the following way

$$-\rho\overline{u_iu_j} = \nu_{TOT}\left(\frac{\partial u_i}{\partial x_j}+\frac{\partial u_j}{\partial x_i}-\frac{2}{3}\frac{\partial u_k}{\partial x_k}\delta_{ij}\right)-\frac{2}{3}\rho k_{TOT}\delta_{ij}, \quad (44)$$

where $\nu_{TOT} = \nu_{T,s}+\nu_{T,l}$ and $k_{TOT} = k_{T,s}+k_{T,l} = k$.

4. Numerical method

The numerical method employed to solve the two-dimensional RANS and transition model equations is described in the following. The system of equations is written in generalized curvilinear coordinates, (ξ,η); a pseudo-time derivative is added to the left-hand side in order to use a time marching approach for the present steady-state problems. The preconditioning matrix, Γ, proposed by Venkateswaran et al. (1992) and Merkle (1995) is finally used to premultiply the pseudo-time derivative in order to improve computational efficiency. The final system reads:

$$\Gamma\frac{\partial Q_v}{\partial\tau}+\frac{\partial E}{\partial\xi}+\frac{\partial F}{\partial\eta}-\frac{\partial E_v}{\partial\xi}-\frac{\partial F_v}{\partial\eta} = D, \quad (45)$$

where $Q_v = (p,u,v,T,k,\omega,\zeta)^T$ is the primitive variable vector, E, F, and E_v, F_v indicate the inviscid and viscous fluxes, respectively, D is the vector of the source terms for the turbulence and transition equations. Notice that the dependent variable ζ is present only for models M4 ($\zeta=\gamma$), M5 ($\zeta=\gamma$), and M6 ($\zeta=k_L$). Discretizing Eq. (45) by the Euler implicit scheme in pseudo-time, the following equation in delta form is obtained:

$$\left[\Gamma+\Delta\tau\frac{\partial}{\partial\xi}\left(\mathbf{A}_v-\mathbf{R}_{\xi\xi}\frac{\partial}{\partial\xi}-\mathbf{R}_{\xi\eta}\frac{\partial}{\partial\eta}\right)+\Delta\tau\frac{\partial}{\partial\eta}\left(\mathbf{B}_v-\mathbf{R}_{\eta\eta}\frac{\partial}{\partial\eta}-\mathbf{R}_{\eta\xi}\frac{\partial}{\partial\xi}\right)\right]\Delta Q_v = -\Delta\tau\mathscr{R}^r, \quad (46)$$

where r and $\Delta\tau$ indicate the pseudo-time level and step, $\mathbf{A}_v = \partial E/\partial Q_v$, $\mathbf{B}_v = \partial F/\partial Q_v$, $\mathbf{R}_{ij}$ are the viscous coefficient matrices (Schwer, 1999), and the matrix Γ is evaluated as proposed by Venkateswaran and Merkle (1995) and Buelow et al. (1997). The residual is given as:

$$\mathscr{R}^r = \frac{\partial(E^r-E_v^r)}{\partial\xi}+\frac{\partial(F^r-F_v^r)}{\partial\eta}-D^r, \quad (47)$$

and the delta unknowns to be annihilated at every pseudo-time level are

$$\Delta Q_v = Q_v^{r+1}-Q_v^r. \quad (48)$$

The left-hand side (LHS) of Eq. (46) is modified to improve the efficiency of the method, without affecting the residual, namely, the physical solution. Firstly, the non-orthogonal viscous coefficient matrices, $\mathbf{R}_{\xi\eta}$ and $\mathbf{R}_{\eta\xi}$, are neglected, and the remaining ones are approximated by the corresponding spectral radii multiplied by the identity matrix, $\mathbf{R}_{\xi\xi} = R_\xi\mathbf{I}$ and $\mathbf{R}_{\eta\eta} = R_\eta\mathbf{I}$. Furthermore, in order to solve the resulting linear system, the diagonalization procedure of Pulliam and Chaussee (1981) is firstly applied, so that the matrices $\mathbf{\Gamma}^{-1}\mathbf{A}_v$ and $\mathbf{\Gamma}^{-1}\mathbf{B}_v$ can be written as:

$$\mathbf{\Gamma}^{-1}\mathbf{A}_v = \mathbf{M}_\xi \Lambda_\xi \mathbf{M}_\xi^{-1}, \quad \mathbf{\Gamma}^{-1}\mathbf{B}_v = \mathbf{M}_\eta \Lambda_\eta \mathbf{M}_\eta^{-1}, \tag{49}$$

where $\mathbf{M}_\xi$, $\mathbf{M}_\eta$ are the right-eigenvector matrices, $\mathbf{M}_\xi^{-1}$, $\mathbf{M}_\eta^{-1}$ are the left-eigenvector matrices; and Λ_ξ and Λ_η are diagonal matrices containing the eigenvalues of $\mathbf{\Gamma}^{-1}\mathbf{A}_v$ and $\mathbf{\Gamma}^{-1}\mathbf{B}_v$, respectively; then, the LHS of Eq. (46) is factorized,

$$\mathbf{\Gamma}\mathbf{M}_\xi \left[\mathbf{I} + \Delta\tau \frac{\partial}{\partial\xi}\left(\Lambda_\xi - R_\xi \mathbf{I}\frac{\partial}{\partial\xi}\right)\right]\mathbf{M}_\xi^{-1}\mathbf{M}_\eta \times \left[\mathbf{I} + \Delta\tau \frac{\partial}{\partial\eta}\left(\Lambda_\eta - R_\eta \mathbf{I}\frac{\partial}{\partial\eta}\right)\right]\mathbf{M}_\eta^{-1}\Delta Q_v = -\Delta\tau \mathscr{R}^r, \tag{50}$$

and solved by a standard scalar alternating direction implicit procedure (Buelow et al., 1997). A cell-centered finite volume space discretization is used on a multi-block structured mesh. A third-order-accurate Steger and Warming flux vector splitting scheme (Steger and Warming, 1981) is employed to discretize the convective terms, the minmod limiter being applied in the presence of shocks, whereas the viscous terms are discretized by second-order-accurate central differences. Further details of the method can be found in Schwer (1999, 2003), the latter also providing the original version of the code developed at the Pennsylvania State University.

Characteristic boundary conditions for the flow variables are imposed at inflow and outflow points, whereas no slip and adiabatic conditions are imposed at the walls. The values of k and ω at inflow points are assigned together with $\gamma = 0$ for models M1–M5, whilst linear extrapolation is used at outflow points; at solid walls $k = 0$ and ω is evaluated using the condition proposed by Menter and Rumsey (1994), $\omega = 60\nu/(\Delta y_1^2 \beta)$, where Δy_1 is the distance of the first cell center from the wall. For model M6, also $k = 0$ and $k_L = 0$ are assigned at solid walls whereas the condition $\partial\omega/\partial n = 0$ is employed for the specific dissipation rate. It is noteworthy that, for stability reasons, the wall boundary conditions assigned to k and k_L are different from those employed by Walters and Leylek (2004) who used Neumann boundary conditions.

All results have been obtained with double-precision computations and are grid converged. The computations have been started considering the fluid at rest, the turbulent and transition quantities being initialized to zero. A residual drop of eight orders of magnitude for the conserved variable equations has been required for convergence, with only the following exceptions: the equation for k_L of model M6, that achieves a residual drop of about four orders of magnitude for all test cases; the equation for γ of model M5, that provides a residual drop of about four orders of magnitude for test cases T3A and T3C2.

5. Results

This section provides the numerical results obtained using the numerical method and the six transition models described above for four well documented test cases: three flows over a flat plate with different free-stream conditions and the more complex flow through a turbine cascade.

5.1. Flows over a flat plate

The test cases proposed by ERCOFTAC SIG 10 (Savill, 1993a,b) have been considered. The experimental data correspond to the flow configurations known as T3A, T3B and T3C2. All tests refer to the transitional flow over an adiabatic flat plate with a sharp leading edge. The first two tests have zero pressure gradient, whereas in the third one the flow experiences a non-zero pressure gradient resulting from the geometry of the wall facing the flat plate (Savill, 1993a,b). The flow conditions corresponding to the three tests are given in Table 1. The Reynolds number is based on the inlet (in) values and the reference length equal to one meter. The turbulence intensity is measured at the section containing the leading edge of the plate. In order to match such values of Tu and the correct decay of the turbulence kinetic energy along the channel, the values of Tu_{in} and $(\mu_T/\mu)_{in}$ provided in Table 2 have been assigned at the inlet section. Needless to say, the transition is strongly influenced by the decay of Tu in the free-stream; therefore, it is very important for a correct analysis of the results to assign the appropriate inlet boundary conditions.

5.1.1. Test cases T3A and T3B

For the first test case, the length of the plate is 1.7 m, whereas the computational domain is a rectangle with dimensions 1.85 m × 0.15 m, its inlet section being located at 0.15 m upstream of the leading edge. The domain is discretized by 140 × 120 stretched cells, so that $y^+ = 0.1$ at the first grid point close to the plate. Figs. 1–7 provide the results obtained using the M1, M4, M5, and M6 transition models for the T3A test case. Models M2 and M3, using a pressure-gradient correction, have not been considered. Fig. 1 shows that a satisfactory matching with the experimental decay of Tu along the channel is achieved. Fig. 2 provides the distribution of the skin-friction coefficient, C_f, along the plate: the numerical results show that, for this test case, correlation C1 provides a delayed onset (corresponding to $Re_{\theta_t} = 198.16$), followed by a too short transition length predicted by model M1. It is noteworthy that models M4 and M5 provide very similar results, Re_{θ_t} being equal to 224.31. Model M6 provides the most accurate

Table 1
ERCOFTAC test cases

	Re	u_{in} (m/s)	Tu (%)	ν_T (m^2/s)
T3A	3.6×10^5	5	3.35	1.48×10^{-5}
T3B	6.3×10^5	9.6	6	1.48×10^{-5}
T3C2	3.5×10^5	5	2.8	1.54×10^{-5}

Table 2
Inlet conditions for the ERCOFTAC test cases

	T3A	T3B	T3C2
Tu_{in} (%)	10	8.2	8.5
$(\mu_T/\mu)_{in}$	0.35	114	0.11

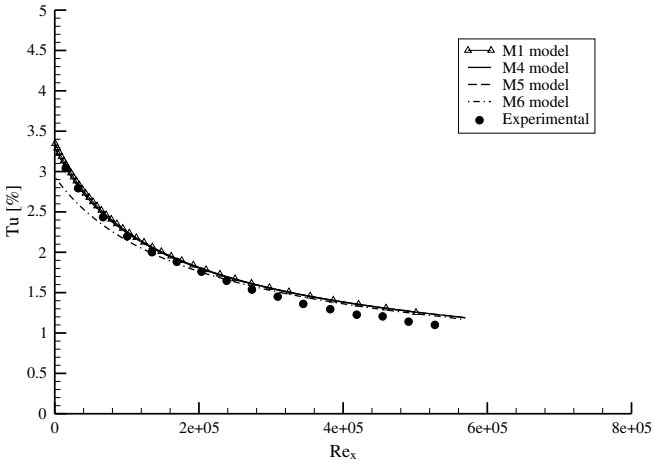

Fig. 1. Free stream turbulence intensity decay for test case T3A.

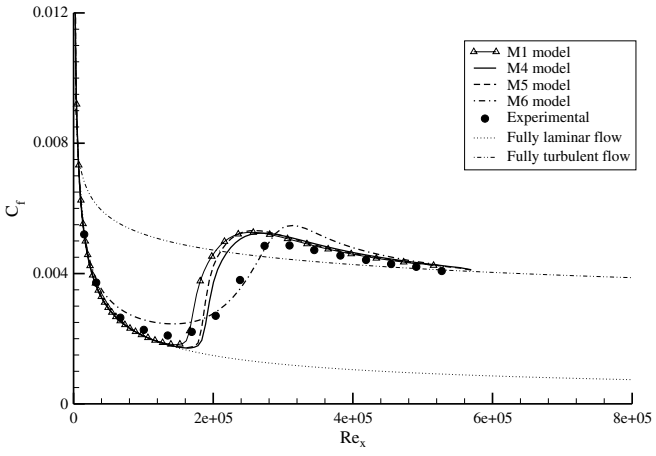

Fig. 2. Skin-friction coefficient for test case T3A.

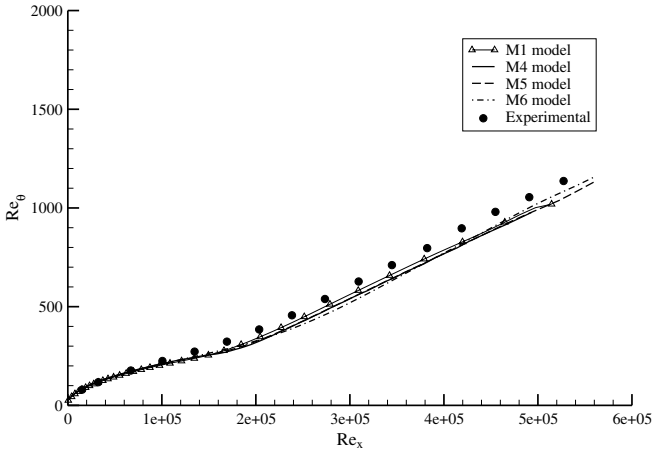

Fig. 3. Re_θ for test case T3A.

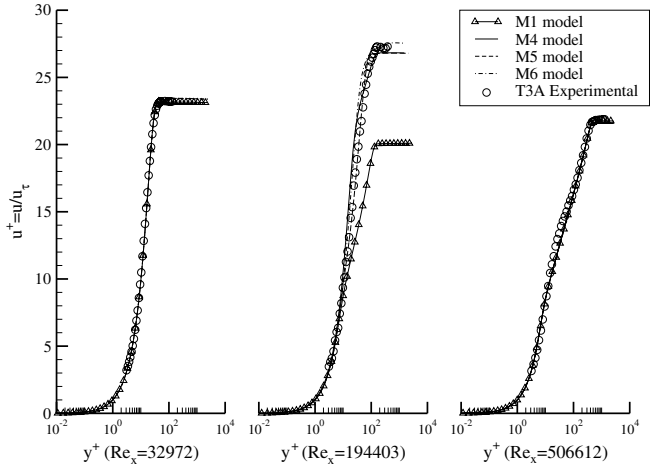

Fig. 4. Boundary-layer profiles for test case T3A.

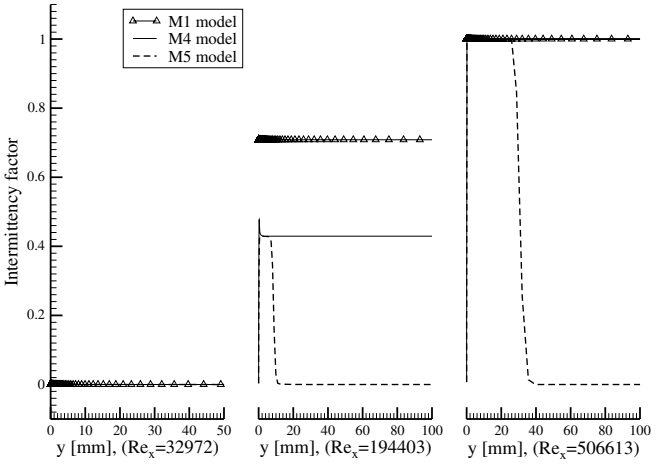

Fig. 5. Intermittency profiles for test case T3A.

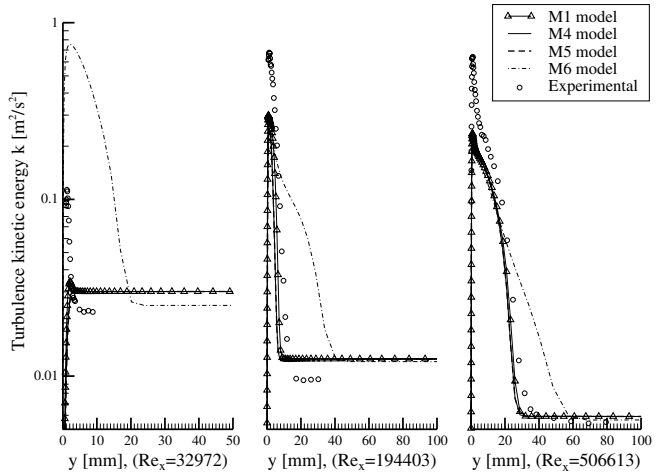

Fig. 6. Turbulence kinetic energy profiles for test case T3A.

predictions for this test case. On the other hand, Fig. 3 does not show any substantial difference among the numerical results obtained using the four models for the Reynolds number based on the momentum thickness, Re_θ. Fig. 4 provides a comparison between the experimental and numerical boundary-layer profiles at three cross-sections along the plate, upstream of, inside, and downstream of

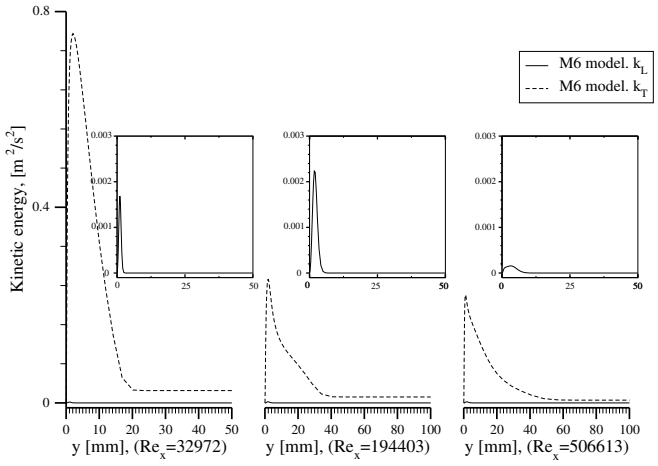

Fig. 7. Kinetic energy profiles for test case T3A and model M6.

the transition region, respectively. It is clear from the velocity profiles at $Re_x = 194{,}403$ that model M1 predicts transition too early, whereas the laminar ($Re_x = 32{,}972$) and turbulent ($Re_x = 506{,}612$) velocity profiles, reported in the same figure, show a good agreement with the experimental data. This is confirmed by the intermittency-factor profiles at the same cross-sections obtained using models M1, M4 and M5 and provided in Fig. 5. The profiles at $Re_x = 194{,}403$ and 506,612 show that model M5, unlike models M1 and M4, reduces to zero the intermittency factor in the free-stream. For completeness, Fig. 6 shows the turbulence kinetic energy profiles at the same cross-sections. From the profiles at $Re_x = 32{,}972$, it is clear that only model M6 has already triggered the transition onset in agreement with the experimental data. Furthermore, Fig. 7 provides the turbulence and laminar kinetic energy profiles for model M6 at the three sections above. The laminar kinetic energy is about two orders of magnitude smaller than the turbulence one and is also reported in the boxes using a different scale. Also the laminar kinetic energy has its peak value very close to the wall at all sections. The test case T3A has been also computed using model M3: Fig. 8 demonstrates that the differences between the algebraic and the intermittency-transport models are negligible, when using the same transition-onset correlation, C2. A final consideration is in order. As previously mentioned, all the results are grid converged. This is confirmed by comparing the distributions of the skin-friction coefficient obtained with models M1, M5 and M6, respectively, using three grids, provided in Figs. 9–11. Therefore the finest mesh can be considered adequate for the test cases T3A, T3B and T3C2, in agreement with the results of Chen et al. (1998) who found a similar mesh to be suitable for such a computation.

For the second test case, labeled T3B, the previous computational grid has been employed. Figs. 12–18 provide the numerical results obtained using the M1, M4, M5, and M6 transition models. Fig. 12 demonstrates that also in this case a satisfactory matching with the experimental decay of *Tu* along the channel is achieved. Fig. 13 provides the distribution of the skin-friction coefficient along the plate: both transition-onset correlations, C1 and C2, predict the

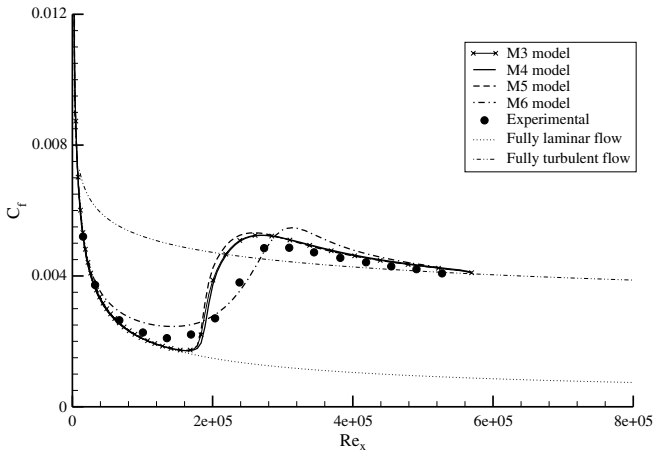

Fig. 8. Skin-friction coefficient for test case T3A.

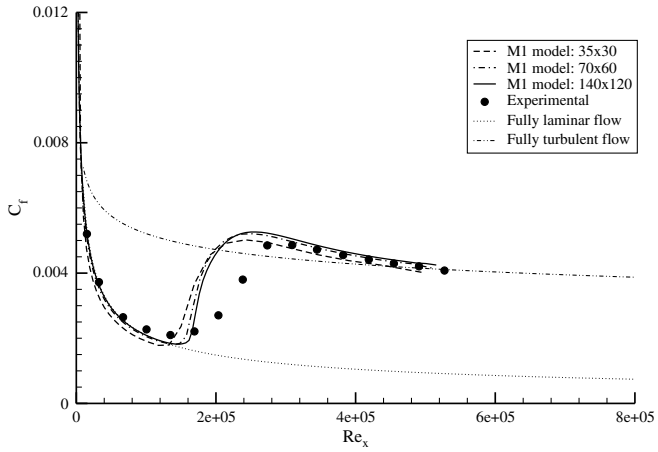

Fig. 9. Skin-friction coefficient for test case T3A: mesh refinement study using M1.

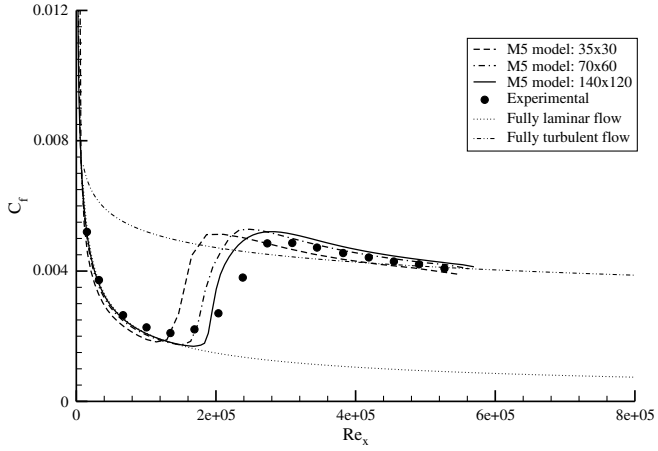

Fig. 10. Skin-friction coefficient for test case T3A: mesh refinement study using M5.

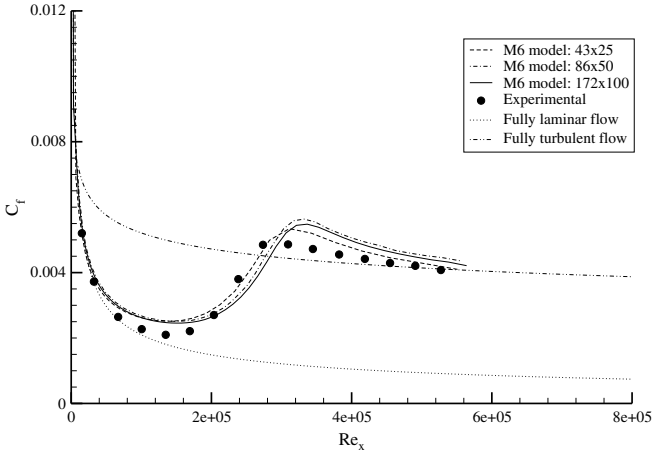

Fig. 11. Skin-friction coefficient for test case T3A: mesh refinement study using M6.

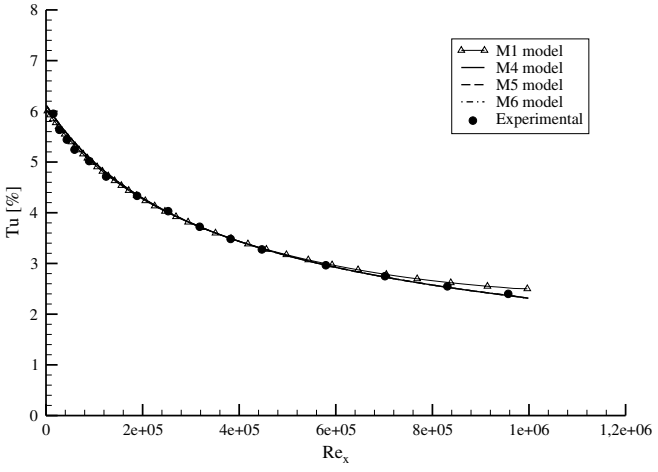

Fig. 12. Free stream turbulence intensity decay for test case T3B.

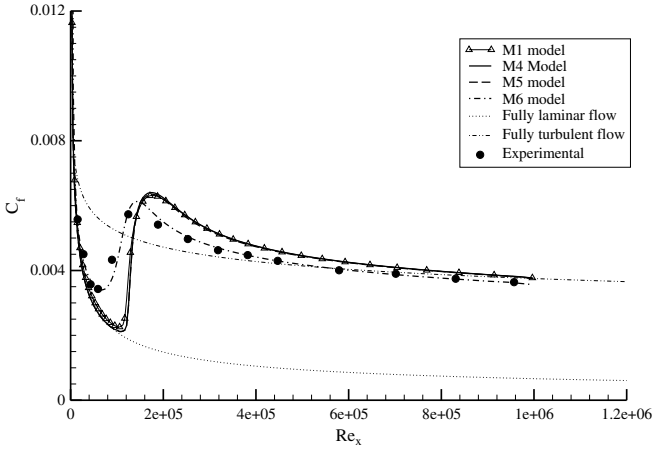

Fig. 13. Skin-friction coefficient for test case T3B.

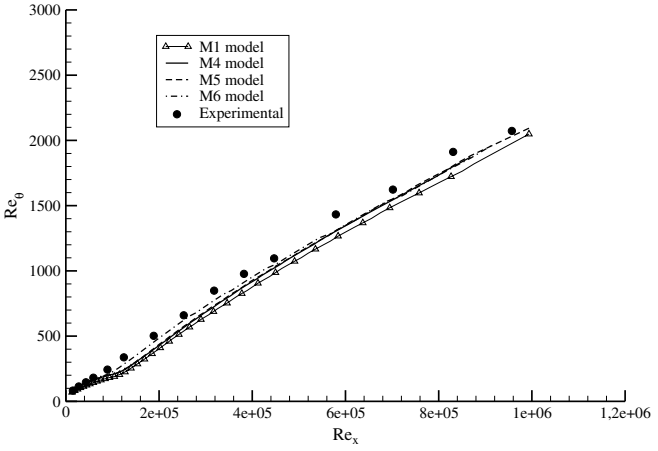

Fig. 14. Re_θ for test case T3B.

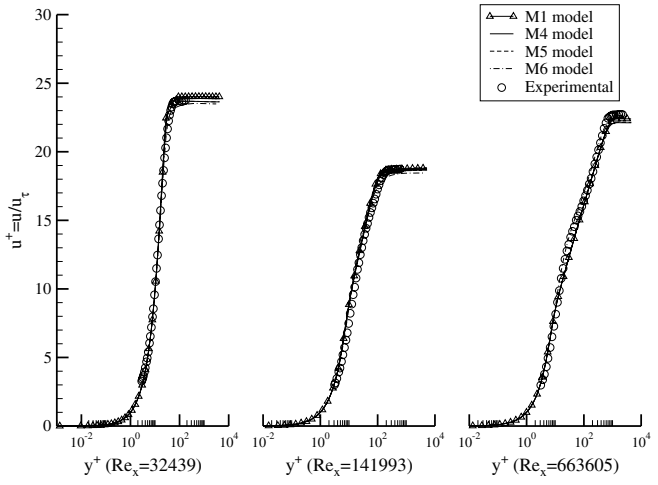

Fig. 15. Boundary-layer profiles for test case T3B.

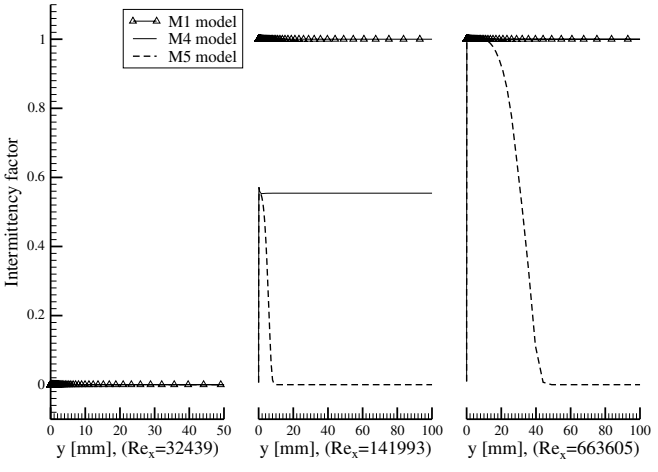

Fig. 16. Intermittency profiles for test case T3B.

transition with a remarkable delay, the numerical results being very close to each other. The Re_{θ_t} values at the transition onset, provided by correlations C1 and C2, are 165.48 and 198.44, respectively. It appears that any of the three models using C1 and C2 cannot predict correctly

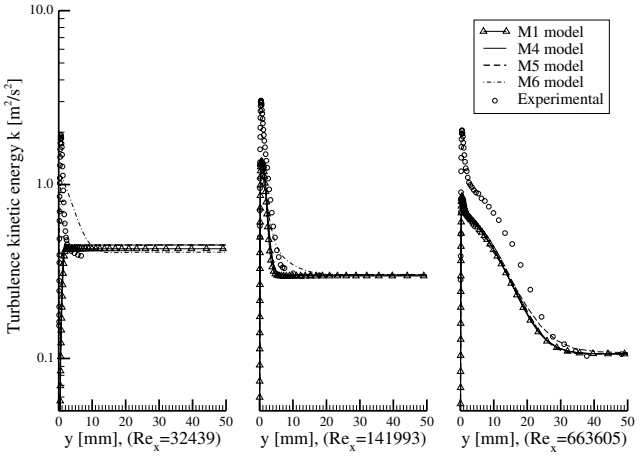

Fig. 17. Turbulence kinetic energy profiles for test case T3B.

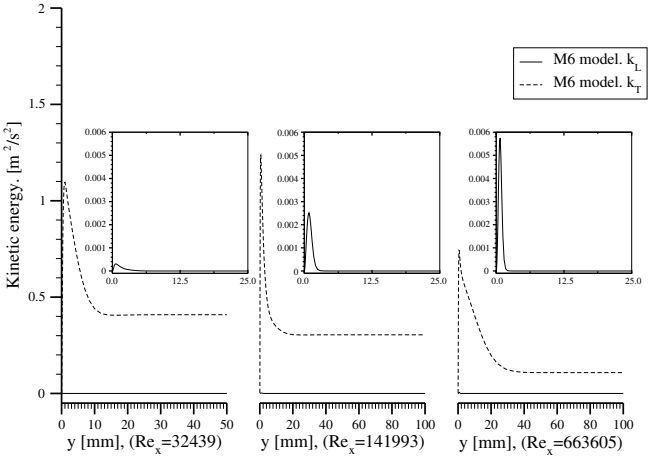

Fig. 18. Kinetic energy profiles for test case T3B and model M6.

the position of the transition onset with the present higher value of the free-stream turbulence. On the other hand, model M6 performs even better than in the previous test, providing the best solution. All models underestimate the value of Re_θ, as shown in Fig. 14; on the other hand, Fig. 15 shows that a satisfactory agreement is obtained for the velocity profiles. For completeness, the intermittency-factor distributions obtained using models M1, M4 and M5 are shown in Fig. 16 and the corresponding turbulence kinetic energy profiles are provided in Fig. 17. Also in this case, from the profiles at $Re_x = 32{,}439$, it is clear that only model M6 has already triggered the transition onset in agreement with the experimental data. Finally, Fig. 18 provides the turbulence and laminar kinetic energy profiles for model M6 at the three sections above. Again the laminar kinetic energy is reported in the boxes using a different scale.

5.1.2. Test case T3C2

For this test case, the length of plate is 1.7 m, whereas that of the computational domain is 1.8 m, its inlet section being located 0.1 m upstream of the leading edge. The flat plate is at the bottom boundary of the domain, whereas the top boundary is shaped according to the ERCOFTAC T3C test geometry, providing a convergent–divergent channel. Such a computational domain is discretized by 202×129 stretched cells so that $y^+ = 0.1$ at the first grid point close to the plate. Figs. 19–25 provide the results obtained using the six transition models. Fig. 19 shows that a satisfactory matching with the experimental decay of Tu along the channel is achieved. Figs. 20 and 21 provide the distributions of the skin-friction coefficient and Re_θ along the plate, respectively. The numerical results show that correlation C1, employed in models M1 and M2, predicts transition too early, whereas correlation C2, employed in the remaining models, is adequate. In fact, the values of Re_{θ_t} provided by correlations C1 and C2 are equal to 226.88 and 263.02, respectively. Moreover, the two intermittency transport models (M4 and M5) provide a more accurate distribution of the skin-friction coefficient in the transition region with respect to the algebraic model M3. It is noteworthy that this test case, due to the flow acceleration, is characterized

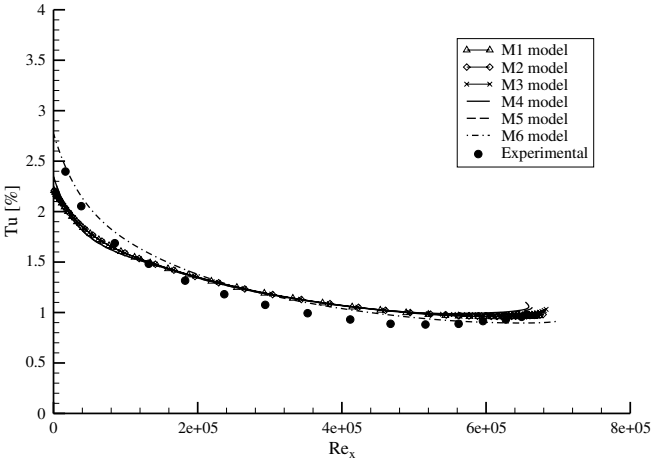

Fig. 19. Free stream turbulence intensity decay for test case T3C2.

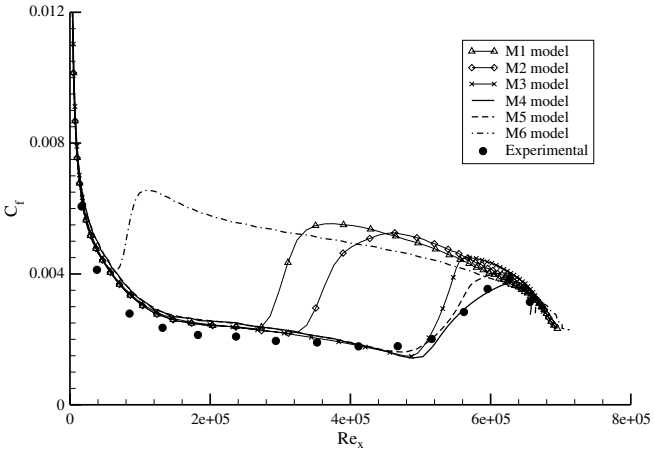

Fig. 20. Skin-friction coefficient for test case T3C2.

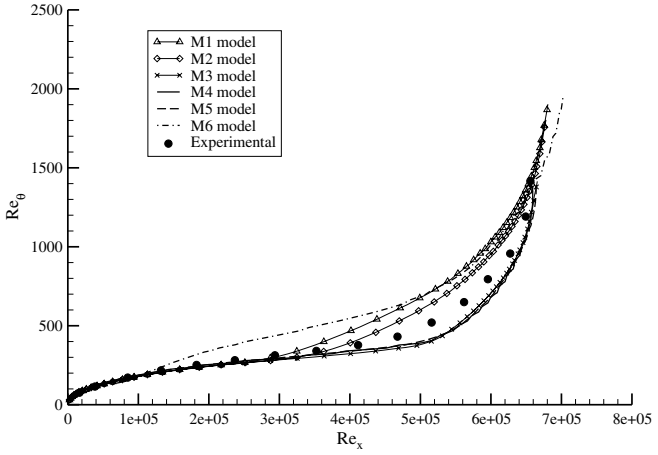

Fig. 21. Re_θ for test case T3C2.

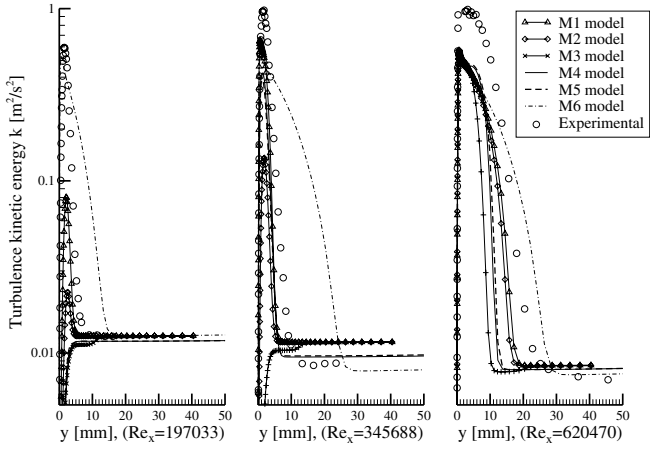

Fig. 24. Turbulence kinetic energy profiles for test case T3C2.

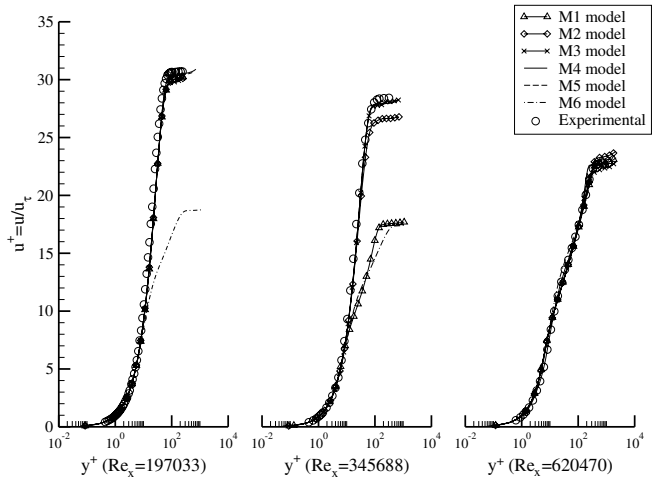

Fig. 22. Boundary-layer profiles for test case T3C2.

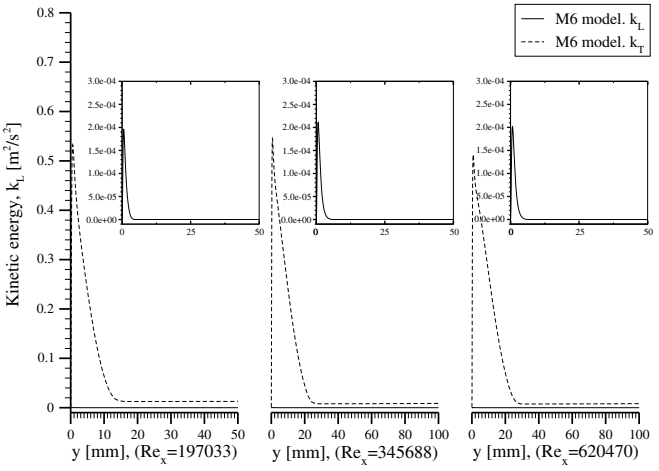

Fig. 25. Kinetic energy profiles for test case T3C2 and model M6.

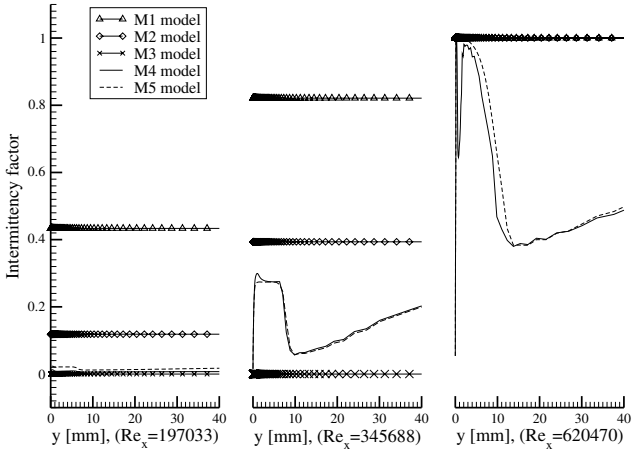

Fig. 23. Intermittency profiles for test case T3C2.

by a large range of Re_x over which the gradient of Re_θ is very small, so that a small error in the prediction of Re_{θ_t} may produce a large error in the prediction of Re_{x_t}: this explains the different behaviours of correlations C1 and C2. On the other hand, the difference between the solutions provided by models M1 and M2 is due to the influence of the pressure gradient correction on the spot production parameter (see Eq. (15)), which delays the growth of the intermittency factor. Finally, it is clearly seen that model M6 is not suitable to predict transition for this test case: the only difference with the previous tests, T3A and T3B, being the presence of the pressure gradient, it can be argued that the model needs to be modified to take into account the effect of the pressure gradient. Finally, Figs. 22–24 provide the velocity profiles, the intermittency factor, and the turbulence kinetic energy, at three cross-sections along the plate, upstream of, inside, and downstream of the transition region. Such data confirm the above results, models M4 and M5 providing profiles which are in good agreement with the experimental data. Finally, Fig. 25 provides the turbulence and laminar kinetic energy profiles for model M6 at the above three sections.

5.2. Turbine cascade

Recently, in order to investigate the effect of the Reynolds number on turbomachinery blade boundary-layer transition, detailed experimental data have been provided by Canepa et al. (2003) and Ubaldi et al. (1996) for the suction side of a high-pressure gas turbine nozzle blade. Its main geometrical features are: chord length $c = 0.3$ m, pitch-to-chord ratio $g/c = 0.7$, blade aspect ratio $h/c = 1$, stagger angle (with respect to the axial direction) $\beta = 49.83°$. With the use of advanced LDV techniques and surface mounted hot-film gauges, the authors give an accurate description of the boundary-layer development and its turbulence characteristics such as boundary-layer profiles, longitudinal distributions of integral parameters, skin-friction coefficient, and turbulence kinetic energy profiles. In this paper, in order to validate the proposed numerical method, the set of experimental data at $Re_{2c} = 590{,}000$ with $M_{2,is} = 0.086$ (Canepa et al., 2003) has been considered. The Reynolds number is based on the exit flow conditions and on the chord length. The upstream turbulence intensity based on the stream-wise velocity fluctuations and inlet velocity is equal to 3%, whereas the integral length scale of turbulence evaluated from the power density spectrum of the stream-wise velocity is equal to 3.7% of the chord length. The two intermittency transport models M4 and M5, and model M6 have been employed for these computations, since they provided the best results for the previous test cases.

Steady flow computations have been performed using a multi-block grid with 22,448 cells and 18 blocks. An O-type grid has been employed around the profile, see Fig. 26, in order to have a quasi orthogonal mesh close to the wall. For the first row of grid points at the wall $y^+_{min} = 0.005$, $y^+_{max} = 0.06$, the average value being $\bar{y}^+ = 0.04$. Fig. 27 provides a comparison between the numerical and experimental distributions of the isentropic velocity along the blade, whereas Fig. 28 shows the Mach number contours. Both numerical results are coincident within plotting accuracy for the three employed models. According to the measurements provided by Canepa et al. (2003), at this rather low Reynolds number, the transition region is very short and the boundary layer on the suction side is laminar until $x/x_{max} = 0.55$. This is supported by the analysis of the distributions along the suction side of the boundary-layer parameters provided in Figs. 29–32, which show the skin-friction coefficient, C_f, the displacement thickness, $\delta^\star$, the momentum thickness, θ, and the shape factor, H_{12}, respectively. Upstream of the start of transition, namely at

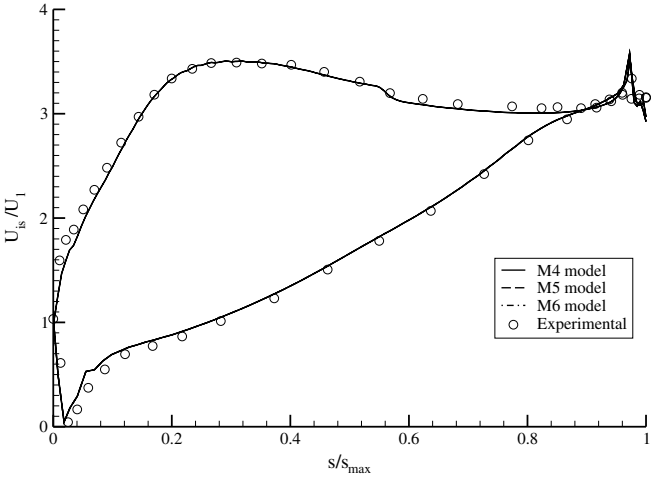

Fig. 27. Isentropic velocity distribution along the profile.

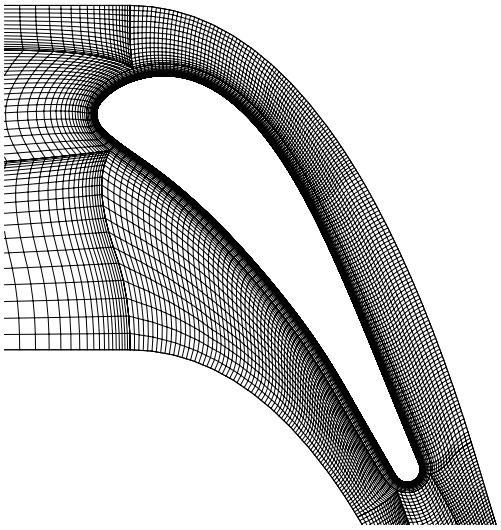

Fig. 26. Multi-block grid for the turbine cascade.

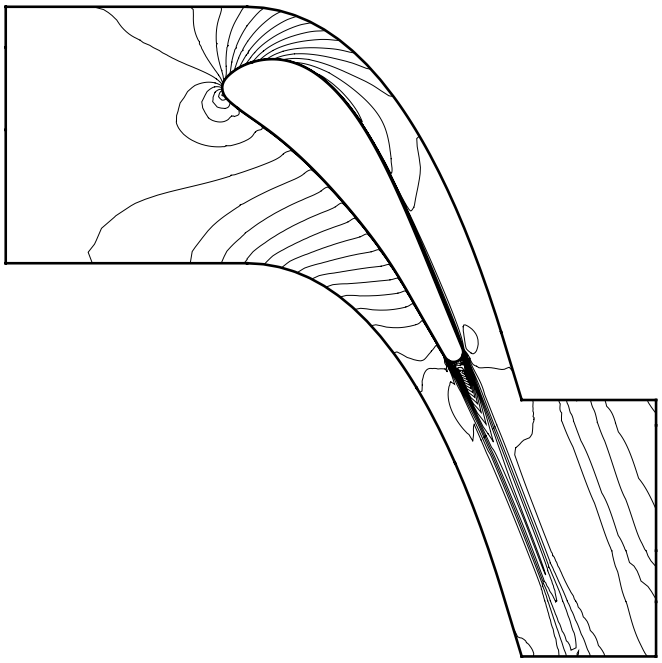

Fig. 28. Mach number contours ($\Delta M = 0.005$, $M_{max} = 0.1$).

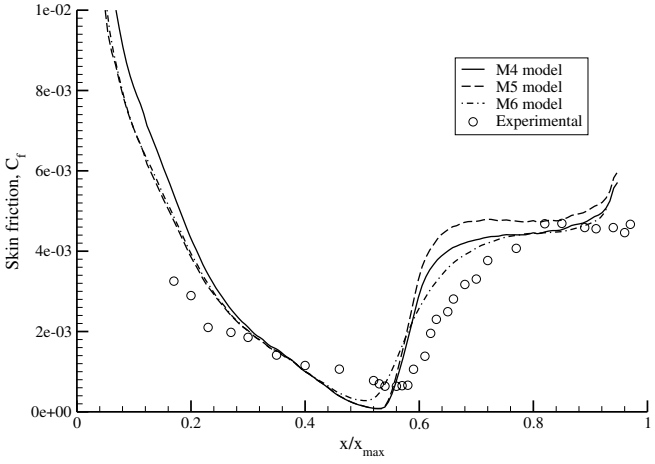

Fig. 29. Skin-friction coefficient ($Re = 5.9 \times 10^5$).

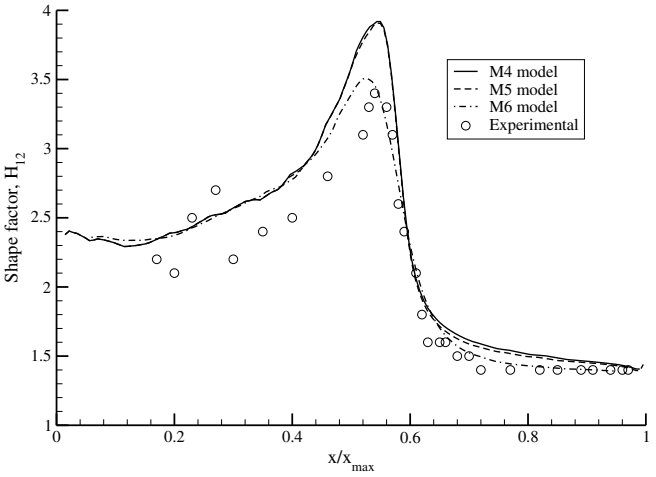

Fig. 32. Shape factor ($Re = 5.9 \times 10^5$).

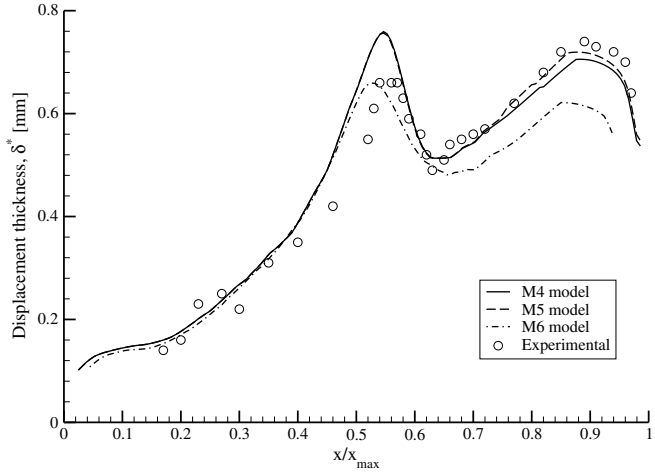

Fig. 30. Displacement thickness ($Re = 5.9 \times 10^5$).

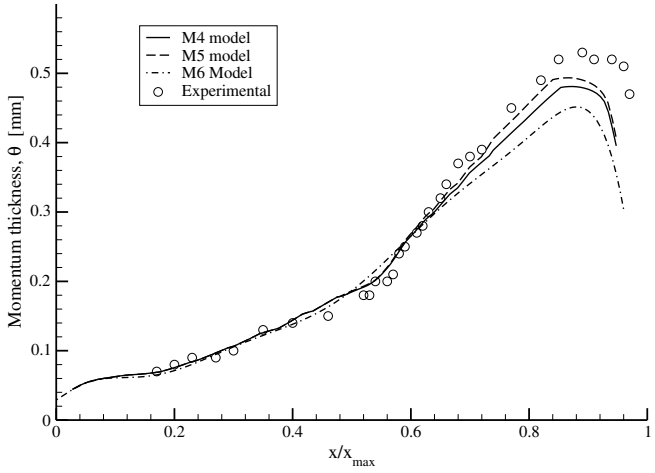

Fig. 31. Momentum thickness ($Re = 5.9 \times 10^5$).

$0.45 < x/x_{max} < 0.55$, $\delta^\star$ and H_{12} show a typical steep increase, indicating an incipient separation which is suppressed by the transition, as clearly seen by the sudden decrease of $\delta^\star$ and H_{12}. The length of the transition region is approximately equal to 15% of the suction side surface length. The three transition models provide numerical results in good agreement with the experimental data. In particular, the momentum thickness distribution is very well predicted, including the value at the transition onset. From the behaviour of $\delta^\star$ and H_{12} it appears that the displacement thickness upstream of the transition region, computed using models M4 and M5, is greater than that provided by the experimental data. This is probably due to the lack of modeling of the interaction between the free-stream turbulence and the laminar boundary layer (this will be seen in the following analysis of the turbulence kinetic energy profiles). However, the predicted length of the transition region is in good agreement with the experimental data. On the other hand, model M6 provides an improved prediction of the peak values of $\delta^\star$ and H_{12} in the pretransitional region at $x/x_{max} \approx 0.5$. At a first glance, one could consider surprising that model M6 provides such accurate results whereas for the previous T3C2 test case, in the presence of a pressure gradient, the results were disappointing. This behaviour may be explained considering that the transition for the turbine flow is located in a region with mild pressure gradient, as shown in Fig. 27. Fig. 33 provides the comparison of the measured and computed velocity profiles at 12 cross-sections in the boundary layer along the suction side. The agreement between numerical and experimental data appears good. All characteristics of laminar, transitional and turbulent profiles are well captured by the present numerical method, in particular it appears that at $x/x_{max} = 0.46$ the flow is in condition of incipient separation just before the transition onset. Finally, Fig. 34 shows the profiles of the turbulence kinetic energy along the suction side. The first five profiles demonstrate that the present numerical model cannot capture the turbulence fluctuations in the laminar boundary layer induced by the free-stream turbulence. After the transition onset, the numerical results agree qualitatively well

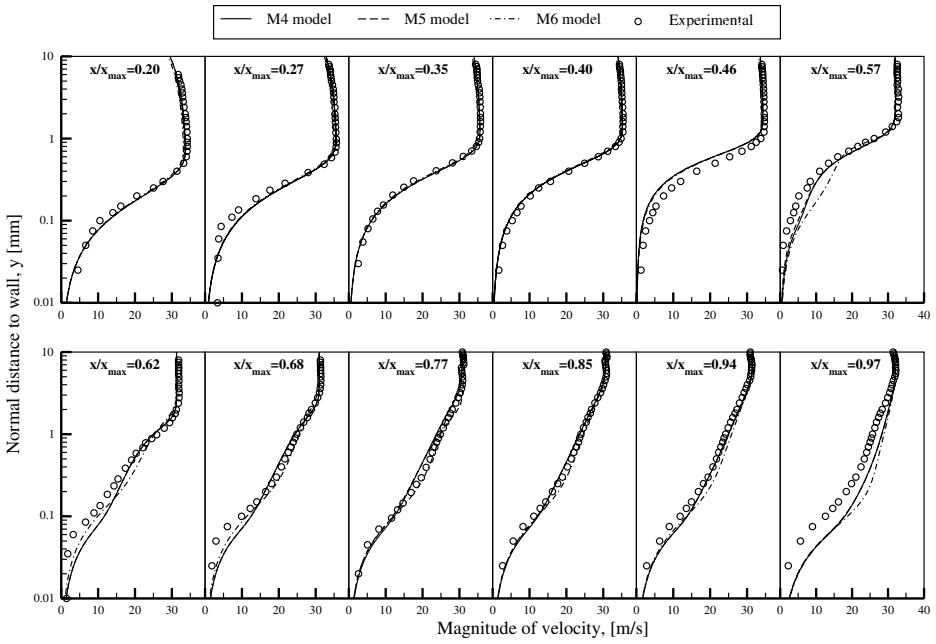

Fig. 33. Velocity profiles ($Re = 5.9 \times 10^5$).

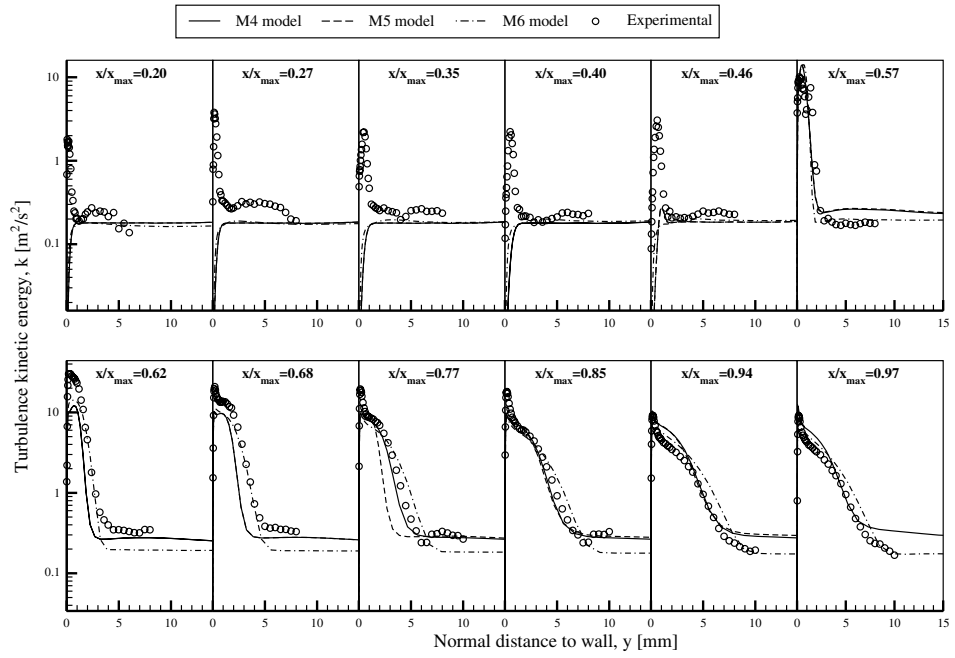

Fig. 34. Turbulence kinetic energy profiles ($Re = 5.9 \times 10^5$).

with the experimental data, the peak vales of k at $0.62 \leqslant x/x_{\max} \leqslant 0.85$ being under-estimated by models M4 and M5 and correctly predicted by model M6.

6. Conclusions

This paper provides an evaluation of six laminar-to-turbulent bypass transition models. Five models are obtained by combining a transition-onset correlation with an intermittency-factor model; whereas the last one is a single-point model based on the use of a laminar kinetic energy transport equation. Such models have been embedded in a Reynolds averaged Navier–Stokes solver employing a low Reynolds number k–ω turbulence model. The performance of the models have been evaluated at first by computing three well documented incompressible flows

over a flat plate, namely, tests T3A, T3B, and T3C2 of ERCOFTAC SIG 10, with different free-stream conditions, the last one being characterized by non-zero pressure gradient. Then, the two-dimensional flow through a linear turbine cascade has been considered, for which detailed experimental data are available in the literature. From the above computations the following conclusions can be drawn:

(1) The employed transition-onset correlations are not satisfactory in the considered range of values of turbulence intensity, *Tu*, insofar as they show a tendency to delay transition, especially as *Tu* increases.
(2) In the presence of non-zero pressure gradients: (i) the transition-onset correlation of Suzen et al. (C2) provides more accurate results than those obtained by the correlation of Abu-Ghannam and Shaw, the latter predicting an early transition onset; (ii) the intermittency-transport models provide more accurate results with respect to the simpler algebraic correlation of Dhawan and Narasimha.
(3) For all of the considered test cases, the intermittency-transport models due to Steelant and Dick and Suzen and Huang provide very similar results.
(4) Model M6 always provides the best results except for the T3C2 test case. This may be due to the presence of a strong pressure gradient in the transition region. The model needs to be modified to take into account the effect of the pressure gradient.
(5) The more complex turbine-flow test case shows the need for including the effect of the free stream turbulence on the laminar boundary layer. For this reason, model M6 provides improved results with respect to models M4 and M5.

Acknowledgments

This research has been supported by the MIUR and the Politecnico di Bari, grants CofinLab 2000 (CEMeC) and Cofin 2003. The authors are grateful to their colleagues of the University of Genova for providing detailed experimental data for the turbine-flow test case.

References

Abu-Ghannam, B.J., Shaw, R., 1980. Natural transition of boundary layers – the effect of turbulence, pressure gradient and flow history. J. Mech. Eng. Sci. 22 (5), 213–228.

Buelow, P.E.O., Schwer, D.A., Feng, J.-Z., Merkle, C.L., Choi, D., 1997. A preconditioned dual time diagonalized ADI scheme for unsteady computations. AIAA Paper 97-2101.

Canepa, E., Cattanei, A., Pittaluga, F., Ubaldi, M., Zunino, P., 2003. Transitional boundary layer on the suction side of a turbine blade at different Reynolds numbers. In: 5th European Conference on Turbomachinery, Praha.

Chen, W.L., Lien, F.S., Leschziner, M.A., 1998. Non-linear eddy-viscosity modelling of transitional boundary layers pertinent to turbomachine aerodynamics. Int. J. Heat Fluid Flow 19, 297–306.

Cho, R., Chung, M.K., 1992. A k–ε–γ equation turbulence model. J. Fluid Mech. 237, 301–322.

Craft, T.J., Launder, B.E., Suga, K., 1997. Prediction of turbulent transitional phenomena with a nonlinear eddy-viscosity model. Int. J. Heat Fluid Flow 18, 15–28.

De Palma, P., 2002. Accurate numerical simulation of compressible turbulent flows in turbomachinery. AIAA J. 40 (4), 702–708.

De Palma, P., Pascazio, G., Napolitano, M., 2001. Accurate and efficient solutions of unsteady viscous flows. Int. J. Numer. Methods Heat Fluid Flow 11 (4), 286–307.

Dhawan, S., Narasimha, R., 1958. Some properties of boundary layer during the transition from laminar to turbulent flow motion. J. Fluid Mech. 3, 418–438.

Hanialić, K., Jakirlić, S., Hadzić, I., 1997. Expanding the limits of "equilibrium" second-moment turbulence closures. Fluid Dyn. Res. 20, 25–41.

Mayle, R.E., 1991. The role of laminar–turbulent transition in gas turbine engines. ASME J. Turbomach. 113, 509–537.

Mayle, R.E., Schulz, A., 1997. The path to predicting bypass transition. ASME J. Turbomach. 119, 405–411.

Menter, F.R., Rumsey, C.L., 1994. Assessment of two-equation turbulence models for transonic flows. AIAA Paper 94-2343.

Merkle, C.L., 1995. Preconditioning methods for viscous flow calculations. In: Hafez, M., Oshima, K. (Eds.), Computational Fluid Dynamics. John Wiley & Sons, pp. 419–436.

Michelassi, V., Martelli, F., Dénos, R., Arts, T., Sieverding, C.H., 1999. Unsteady heat transfer in stator–rotor interaction by two-equation turbulence model. ASME J. Turbomach. 121, 436–447.

Pulliam, T.H., Chaussee, D.S., 1981. A diagonal form of an implicit factorization algorithm. J. Comput. Phys. 39, 347–363.

Savill, A.M., 1993a. Further progress in the turbulence modeling of bypass transition. In: Rodi, W., Martelli, F. (Eds.), Engineering Turbulence Modeling and Experiments 2. Elsevier Science, pp. 583–592.

Savill, A.M., 1993b. Some recent progress in the turbulence modeling of by-pass transition. In: So, R.M.C., Speziale, C.G., Launder, B.E. (Eds.), Near-Wall Turbulent Flows. Elsevier Science, pp. 829–848.

Savill, A.M., 2002a. By-pass transition using conventional closures. In: Launder, B., Sandham, N. (Eds.), Closure Strategies for Turbulent and Transitional Flows. Cambridge University Press, pp. 464–492.

Savill, A.M., 2002b. New strategies in modelling by-pass transition. In: Launder, B., Sandham, N. (Eds.), Closure Strategies for Turbulent and Transitional Flows. Cambridge University Press, pp. 493–521.

Schwer, D.A., 1999. Numerical Study of Unsteadiness in Non-reacting and Reacting Mixing Layers. PhD Thesis, The Pennsylvania State University.

Schwer, D.A., 2003. Diagonalized upwind Navier Stokes code. Available from: <http://duns.sourceforge.net>.

Steelant, J., Dick, E., 1996. Modeling of bypass transition with conditioned Navier–Stokes equations coupled to an intermittency transport equation. Int. J. Numer. Methods Fluids 23, 193–220.

Steger, J.L., Warming, R.F., 1981. Flux vector splitting of the inviscid gas-dynamic equations with applications to finite difference methods. J. Comput. Phys. 40, 263–293.

Suzen, Y.B., Huang, P.G., 2000. Modeling of flow transition using an intermittency transport equation. ASME J. Fluids Eng. 122, 273–284.

Suzen, Y.B., Xiong, G., Huang, P.G., 2002. Predictions of transitional flows in low-pressure turbines using an intermittency transport equations. AIAA J. 40 (2), 254–266.

Ubaldi, M., Zunino, P., Campora, U., Ghiglione, A., 1996. Detailed velocity and turbulence measurements of the profile boundary layer in a large scale turbine cascade. In: 96-GT-42, International Gas Turbine and Aeroengine Congress and Exhibition, Birmingham.

Venkateswaran, S., Merkle, C.L., 1995. Dual time stepping and preconditioning for unsteady computations. AIAA Paper 95-0078.

Venkateswaran, S., Weiss, S., Merkle, C.L., Choi, Y.H., 1992. Propulsion related flow fields using the preconditioned Navier–Stokes equations. AIAA Paper 92-3437.

Volino, R.J., 1998. A new model for free-stream turbulence effects on boundary layers. ASME J. Turbomach. 120, 613–620.

Walters, D.K., Leylek, J.H., 2004. A new model for boundary-layer transition using a single-point RANS approach. ASME J. Turbomach. 126, 193–202.

Walters, D.K., Leylek, J.H., 2005. Computational fluid dynamics study of wake-induced transition on a compressor-like flat plate. ASME J. Turbomach. 127, 52–63.

Westin, K.J.A., Henkes, R.A.W.M., 1997. Application of turbulence models to bypass transition. ASME J. Fluids Eng. 119, 859–866.

Wilcox, D.C., 1998. Turbulence Models for CFD. DCW Industries, Inc.